

Atomic Resolution Imaging of Nanoscale Chemical Expansion in $\text{Pr}_x\text{Ce}_{1-x}\text{O}_{2-\delta}$ During *In Situ* Heating

Jessica G. Swallow,[†] Ja Kyung Lee,[‡] Thomas Defferriere,[†] Gareth Martin Hughes,[‡]
Shilpa N. Raja,[†] Harry L. Tuller,[†] Jamie H. Warner,^{*,‡,¶} and Krystyn J. Van
Vliet^{*,†,§}

[†]*Department of Materials Science and Engineering, Massachusetts Institute of Technology,
Cambridge, MA, 02139*

[‡]*Department of Materials, University of Oxford, Oxford, OX1 3PH, UK*

[¶]*Current address: Department of Materials, University of Oxford, 16 Parks Rd., OX1
3PH, UK*

[§]*Current address: 77 Massachusetts Avenue, 8-237, Cambridge, MA, 02139, USA*

E-mail: jamie.warner@materials.ox.ac.uk; krystyn@mit.edu

Abstract

Thin film non-stoichiometric oxides enable many high temperature applications including solid oxide fuel cells, actuators, and catalysis. Large concentrations of point defects (particularly, oxygen vacancies) enable fast ionic conductivity or gas exchange kinetics in these materials, but also manifest as coupling between lattice volume and chemical composition. This chemical expansion may be either detrimental or useful, especially in thin film devices that may exhibit enhanced performance through strain engineering or decreased operating temperatures. However, thin film non-stoichiometric

oxides can differ from bulk counterparts in terms of *operando* defect concentrations, transport properties, and mechanical properties. Here we present an *in situ* investigation of atomic-scale chemical expansion in $\text{Pr}_x\text{Ce}_{1-x}\text{O}_{2-\delta}$ (PCO), a mixed ionic-electronic conducting oxide relevant to electrochemical energy conversion and high temperature actuation. Through a combination of electron energy loss spectroscopy and transmission electron microscopy with *in situ* heating, we characterized chemical strains and changes in oxidation state in cross-sections of PCO films grown on yttria stabilized zirconia (YSZ) at temperatures reaching 650°C. We quantified, both statically and dynamically, the nanoscale chemical expansion induced by changes in PCO redox state as a function of position and direction relative to the film-substrate interface. Additionally, we observed dislocations at the film-substrate interface, as well as reduced cation localization to threading defects within PCO films. These results illustrate several key aspects of atomic-scale structure and mechanical deformation in non-stoichiometric oxide films that clarify distinctions between films and bulk counterparts, and that hold several implications for *operando* chemical expansion or "breathing" of such oxide films.

Keywords

Chemical expansion, non-stoichiometric oxide, *in situ* transmission electron microscopy, chemomechanics

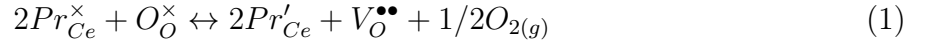
Non-stoichiometric oxides that support very large point defect concentrations are active materials in diverse applications including solid oxide fuel cells (SOFCs), electrolyzers, high temperature oxide actuators, catalysts, and gas sensors.¹⁻⁴ Generally, the point defects that provide the *non-stoichiometry* in these materials are oxygen vacancies that foster important functional properties including fast ionic conductivity and/or oxygen exchange kinetics. Formation, annihilation, and migration of these defects also tend to be coupled to material volume, manifest as chemical expansion or lattice volume coupled to defect content. Chemical expansion is a well-known feature of many non-stoichiometric oxides including fluorites, per-

ovskites, and Ruddlesden-Popper phases.⁵⁻⁷ It is often cited as a source of mechanical failure because it can produce undesired stress or strain in layered systems *in situ*.⁸ Such chemomechanical coupling need not always be a negative effect, however. In fact, electrochemically stimulated chemical expansion in such oxides can be used for high temperature actuation in extreme environments.² Further, in some cases this volume coupled to chemistry may be used to improve device performance, for example by using tensile strain to decrease oxygen vacancy formation energies and thereby enhance exchange kinetics or diffusivity.⁹⁻¹¹ This concept, known as strain engineering, has the potential to decrease the operating temperature of thin film SOFCs or related devices without sacrificing energy conversion efficiency.¹² In fact, the use of thin film non-stoichiometric oxides extends beyond electrochemical energy conversion and storage applications; resistive switches and gas separation membranes may also benefit from miniaturized dimensions.^{4,13}

Leveraging or engineering such chemical expansion effects *in situ*, particularly for applications including strain-engineered SOFC cathodes or high-temperature oxide actuators, requires detailed understanding of how stress and strain develop near mechanically-constrained interfaces *in situ*. Both the uniformity and magnitude of such effects are important, especially at length scales <100 nm that describe line defect contributions to deformation and the elementary steps of charge or mass transfer in the atomic lattice. Here we characterized *in situ* the atomic-scale response of a non-stoichiometric oxide film to elevated temperature up to 650°C and distinct oxidation states, through high resolution transmission electron microscopy (TEM) and electron energy loss spectroscopy (EELS). This non-stoichiometric oxide, Pr-doped ceria or $\text{Pr}_x\text{Ce}_{1-x}\text{O}_{2-\delta}$ (PCO), holds particular promise for high temperature oxide actuators because it exhibits large chemical strain coupled to relatively modest applied voltages ($\sim 0.1\%$ strain per 100 mV) at temperatures above 550°C.² A model mixed ionic-electronic conducting oxide, PCO has been well-characterized in terms of defect chemistry, oxygen exchange kinetics, chemical expansion coefficient, and elastic properties.^{6,14-16} PCO exhibits the fluorite crystal structure widely used in SOFC and oxygen storage applications

and a large chemical expansion coefficient of 0.087 ($\Delta\epsilon/\Delta\delta$).⁶ Therefore, PCO is an ideal model system for understanding thin film chemical expansion effects at the atomic scale.

Equation 1 describes the oxygen vacancy formation reaction in the model non-stoichiometric oxide material $\text{Pr}_x\text{Ce}_{1-x}\text{O}_{2-\delta}$ (PCO) using Kröger-Vink notation, where Pr_{Ce}^\times and Pr'_{Ce} denote Pr^{4+} and Pr^{3+} , respectively, on Ce sites, O_O^\times denotes O^{2-} on an oxygen site, and $V_O^{\bullet\bullet}$ denotes a net double positively charged vacancy on an oxygen site:



Equation 1 exemplifies the oxygen vacancy formation reactions that occur in conjunction with chemical expansion in most non-stoichiometric oxide materials. Increased volume arises from the increased size of the two reduced cations on the right side of Eq. 1, despite the slight volumetric contraction that occurs around the oxygen vacancy.¹⁷ In general, increased charge localization to these cations can be expected to increase the chemical expansion coefficient α_c that couples chemical strain ϵ to change in oxygen vacancy concentration $\Delta\delta$ according to Eq. 2, suggesting that it may be possible to tune this coefficient by cation substitution.¹⁸

$$\epsilon = \alpha_c \Delta\delta \quad (2)$$

The coefficient α_c is assumed generally to be independent of temperature, but this is not always the case.⁵ Additionally, the value of α_c can vary between bulk and thin film forms of the same oxide, and may be anisotropic.^{6,19–22}

Thin films exhibit two important differences from bulk counterparts of the same material: (1) relatively higher densities of crystallographic defects, and (2) influence of mechanical constraints at the film-substrate interface. These differences hold particular importance in non-stoichiometric oxide films such as Pr-doped CeO_2 considered herein. The potential for higher defect density in thin films is attributed generally to the relative contribution of surfaces and interfaces, which naturally comprise a larger proportion of material volume in thin

film specimens. For example, TEM and EELS experiments have shown that CeO_2 films and nanoparticles can exhibit especially large oxygen vacancy concentrations near free surfaces, or exhibit regions enriched in reduced cations in space charge layers at grain boundaries or interfaces.^{23–25} Furthermore, additional capacity for inducible film stress due to thermal or chemical stimuli is attributed to the fact that films adhered to substrates are constrained from lateral displacement and strain at the film-substrate interface. At the atomic scale, this constraint can also include strain associated with film deposition, including atomic lattice mismatch between the two materials. In the context of thermal and chemical expansion, this constraint of lateral displacement with respect to bulk forms of the same material induces additional film strain (or stress) that depends on relative magnitude of thermal or chemical expansion coefficients describing lattice parameter changes as a function of temperature T or point defect content, respectively.

Non-stoichiometric oxide films can also exhibit lattice strain as the point defect content changes *in situ*, including changes in concentrations of reduced cations and corresponding oxygen vacancies. Interfacial constraint may cause most of this environment-dependent lattice strain to occur perpendicular to the interface. This anisotropy in lattice parameter as a function of distance from the film-substrate interface could result plausibly in anisotropic physical and mechanical properties including charge transport and elastoplastic properties. It is of interest to determine to what extent stress-relief mechanisms, such as anisotropic chemical strain, line defect motion, or phase separation, occur and contribute to non-stoichiometric oxide films at high temperatures. Such direct observations are important particularly to discern whether linear defects, phase changes, or spatially anisotropic strains may also couple to other important functional properties of these oxides.

Atomic resolution electron microscopy can provide such a direct means of characterizing chemical expansion *in situ*.^{26,27} There are two main types of atomic-resolution electron microscopy, each with distinct advantages, that are of interest for this purpose, specifically phase contrast transmission electron microscopy (TEM), and scanning transmission electron

microscopy (STEM). The resolution of these techniques has been improving steadily, especially with recent developments in aberration-correction, such that atomic columns can be resolved.^{28,29} STEM is often available in combination with electron energy loss spectroscopy (EELS) that can be used to identify elemental composition as well as oxidation states.^{30–32} Atomic resolution images enable local lattice strain detection through a combination of selected area diffraction (SAD) and geometric phase analysis (GPA, translation of local fast Fourier transform (FFT) information throughout an image to identify strain states relative to a user-specified reference state³³). Because chemical expansion is characterized by both a change in lattice parameter *and* a change in oxidation state, high resolution STEM with EELS provides a powerful method of characterizing this effect at the atomic level.^{33,34}

PCO exhibits both chemical expansion and key discrepancies between film and bulk properties. For example, PCO films exhibit higher oxygen vacancy concentrations than bulk counterparts of the same nominal composition under the same operating conditions.³⁵ PCO films grown on yttria stabilized zirconia (YSZ, a common choice of SOFC electrolyte) have exhibited irreversible stress relaxation at high temperature that is not yet explained fully.²⁰ Additionally, PCO films have shown a stronger dependence of Young’s elastic modulus E on temperature and oxygen partial pressure pO_2 than expected based on modeling of bulk PCO or inferred from measurements of the related oxide $Gd_xCe_{1-x}O_{2-\delta}$.¹⁶ Specifically, E decreased with increased T and decreased oxygen partial pressure pO_2 as the oxide exhibited thermal and chemical expansion, an effect that could be magnified by both increased changes in reduced cation content (and/or associated oxygen vacancy content δ) for a fixed change in environmental conditions, or anisotropic chemical strain resulting from constrained deformation. Thus, PCO films grown on YSZ substrates (as we analyzed in the current study) can be expected to exhibit microstructural and nanoscale features that facilitate these observations and may be observed with high temperature atomic-resolution microscopy.

Several previous studies of undoped and Pr-doped CeO_2 at room temperature have been conducted by TEM, STEM, and EELS. Sheth *et al.* reported that PCO films grown by

pulsed laser deposition (PLD) on YSZ substrates exhibited partial epitaxy with threading dislocations observable *via* TEM that propagated from the interface to the (100)-oriented film surface.²⁰ Those authors also reported irreversible stress relaxation observed by multi-beam optical stress sensors at high temperature for which the mechanisms were not elucidated.²⁰ Several groups have reported misfit dislocations in CeO_2 films grown epitaxially on YSZ.^{24,36,37} Sinclair *et al.* also noted that substantial electron beam exposure for very thin (~ 11 nm) CeO_2 membranes induced vacancy ordering and sample reduction that could be recovered readily with re-oxidation of the sample.³⁶ Vacancy ordering can also be induced in CeO_2 films at room temperature by application of volt-scale electrical bias, a type of *in situ* TEM that recently has been applied to the study of resistive switching effects in non-stoichiometric oxide materials at room temperature.^{32,38,39}

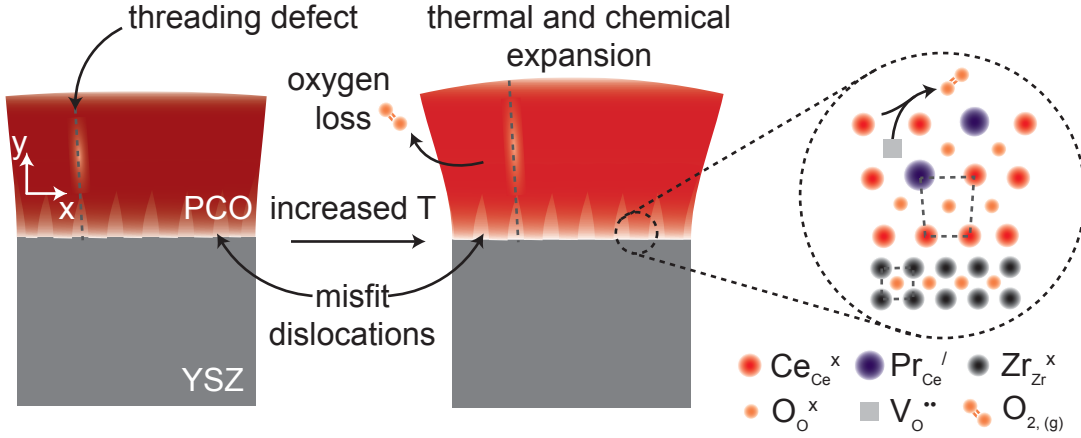


Figure 1: Schematic of *in situ* TEM experiments on non-stoichiometric oxide film cross-sections. Epitaxial $\text{Pr}_{0.1}\text{Ce}_{0.9}\text{O}_{2-\delta}$ (PCO) films grown on yttria stabilized zirconia (YSZ) substrates subject to mechanical constraint at interface. Upon heating inside microscope, PCO films exhibit anisotropic thermal and chemical expansion and associated sample reduction (indicated by lighter film color) through oxygen loss. Defects at interface between the film and/or threading throughout the film thickness may contain higher concentrations of reduced cations. PCO strain determined through Fourier transform analysis of electron microscopy images, and oxidation state change identified by electron energy loss spectroscopy.

Others have also reported non-uniform composition or oxidation state in close proximity to grain boundaries, interfaces, and surfaces in doped and undoped CeO_2 at room temper-

ature. CeO_2 nanoparticles exhibited large vacancy concentrations, surface rearrangements, and lattice expansion that could reach up to 7% after sample reduction in hydrogen at high temperatures, an effect that may be enhanced by doping.^{26,40} Room temperature STEM imaging of CeO_2 films grown on YSZ with EELS has shown substantial Ce cation reduction within a 5 nm distance from the interface, consistent with the concept of interfacial space charge.²⁴ Enhanced cation reduction has also been observed within grain boundary cores in sintered Gd/Pr co-doped CeO_2 powders, along with Gd and Pr enrichment at grain boundaries. This observation was correlated with reduced migration energies for oxygen vacancies, representing an important way in which local microstructural features may be used to enhance functional properties (*e.g.*, ionic conductivity) by providing fast-conduction pathways.⁴¹ In that case, cation reduction at the grain boundary was concurrent with depleted oxygen content, indicating that this was not a space-charge effect. Opposite effects might exist proximal to dislocations in doped or undoped CeO_2 ; computational results have indicated that edge dislocations could retard oxide ion diffusion by causing segregation of charged defects.⁴² While those prior studies observed or predicted many types of non-uniform composition or oxidation states in CeO_2 at room temperature, little direct evidence of these effects at high temperatures has been gathered. Further, the correlation of these defect distributions with chemical expansion has been explored only minimally. In fact, while volume-averaged chemical expansion has been observed by diffraction, stress measurements, or probe-based approaches, there exist few reports of defect distribution or chemical expansion at film-substrate interfaces.²⁷

Here we present analysis of defects and displacements in a model PCO-YSZ system, using an *in situ* heating holder with TEM, STEM, and EELS to quantify chemical expansion, composition, and oxidation state of film-substrate cross-sections. We analyzed two cross-sections, one imaged exclusively at room temperature (Sample A), and one imaged using the *in situ* heating holder at temperatures up to 650°C (Sample B). As shown schematically in Fig. 1, we focused particular attention to the role of the interfacial constraint, modes of chemical

expansion accommodation within the defective lattice, and the nature of linear defects that emerge upon film oxidation. These results confer important implications for understanding how epitaxial non-stoichiometric oxide films may respond to interfacial stresses arising from thermal or chemical expansion *operando*, including potential impact on charge transport or reactivity relevant to high-temperature actuation or electrochemical energy conversion.

Results and discussion

Structural characterization of as-grown PCO

We first characterized PCO-YSZ film-substrate cross-sections at room temperature to assess as-deposited PCO microstructure. Figure 2(a) shows a low magnification image of the PCO-YSZ cross-section (Sample A). The film (of initial thickness ~ 200 nm measured by profilometry) exhibited apparently columnar microstructure. However, upon closer inspection, the threading defects propagating from the interface to the surface of the film (highlighted by white arrows) were discerned to be disordered regions and not grain boundaries separating grains of distinct orientations. Distinct grain orientations would appear as rotated or distorted FFT patterns, while doubled spots at the same orientation but slightly differing spacing d indicate epitaxy. We found no evidence of grain rotation or mismatch on either side of these defects; instead the film was oriented in a consistently epitaxial manner extending along the y -axis from the interface toward the free surface of the deposited films. The doubled spots in the FFT at the PCO-YSZ interface shown in Fig. 2(b) support this conclusion; this doubling is typical of the interface. Sheth *et al.*²⁰ observed similar defects in PCO films grown by PLD on YSZ; those authors attributed such image contrast features to threading dislocations. While our microstructure is consistent with those authors' results, the region at the PCO-YSZ interface at room temperature was in general too disordered in our own images of Sample A to resolve specific dislocation cores or Burgers vectors. However, the film lattice was otherwise possible to resolve with atomic resolution, as exemplified by Fig.

2(c).

Figure 2(c) also denotes the notation we use throughout to indicate sample orientation: " x -component" corresponds to the direction parallel to the film-substrate interface, along which PCO displacement is constrained by the substrate, while " y -component" refers to the direction normal to the film-substrate interface and unconstrained in displacement toward the film free surface. We also note here that there existed a layer of atomic disorder (~ 10 nm) at the film free surface in Sample A. Figure 2(a) denotes that region by a dashed line, and our FFT and EELS analysis indicated a larger proportion of reduced cations and larger lattice volume in that region relative to the rest of the film. Those features were indicative of significant film reduction and associated chemical expansion in that area, and thus we attributed the features of that region to damage during sample preparation by focused ion beam (FIB) milling (see Experimental).

We quantified the as-prepared lattice spacing in the PCO film as a function of distance from the interface relative to the lattice spacing in the YSZ substrate within 10 nm of the interface, as shown in Fig. 2(d). Near the interface, strain in the PCO normal to the interface (y -component) was significantly larger than that parallel to the interface (x -component). This difference decreased with increasing distance from the interface and was approximately equal at a distance of ~ 40 nm. This result is expected in that YSZ exhibits a smaller lattice parameter than PCO, such that the PCO x -component lattice parameter near the film-substrate interface is smaller than that of unconstrained bulk PCO. The PCO film strained normal to the interface under this constraint, and this anisotropic lattice distortion was reduced with increasing distance from the interface. We report this PCO lattice parameter change as a ratio with respect to the YSZ lattice parameter because the $\sim 6\%$ lattice mismatch between these materials is well-established, this method allows us to account for image distortion due to tilt in the TEM under different imaging conditions, and because the YSZ lattice parameter at room temperature is a useful reference length in our subsequent experiments that incurred thermal expansion in both the film and substrate lattices

but chemical expansion in only the PCO film lattice. We note here that the as-grown PCO film exhibited relatively invariant composition as a function of distance from the interface, as quantified by EELS. Except for the FIB-damaged region at the film free surface (*i.e.*, maximum distance in y -direction from the interface), neither the cation oxidation state nor the dopant distribution varied significantly throughout the film or near the linear defects. This result is also consistent with the room temperature results of Sheth *et al.*²⁰

Thermochemical strain anisotropy

Having established the as-prepared PCO film structure, we next characterized film response upon a change in temperature or oxidation state. Using the spatial and chemical resolution afforded by STEM imaging coupled to EELS analysis, we imaged a cross-section loaded on a high temperature TEM holder at four conditions of temperature and oxidation state (see Experimental and Fig. 3). Oxygen exchange in PCO begins above 500°C, with the exchange rate increasing at higher temperatures. Therefore, to oxidize or reduce PCO samples, we held them at 650°C using the *in situ* heating holder in oxidizing (air outside the TEM) or reducing (inside TEM vacuum of $<10^{-11}$ atm) environments for at least 30 min prior to imaging. We estimated that the PCO film cross-section of <100 nm thickness would achieve equilibrium with such environmental conditions well within this time frame. To minimize oxygen loss upon re-entry into the TEM vacuum for imaging, we cooled our oxidized samples rapidly to room temperature, preventing further gas exchange. We note here that the YSZ substrate is not active to oxygen exchange, and so we do not expect significant changes in the YSZ oxygen content or associated lattice volume (beyond thermal expansion effects) due to those changes in environmental conditions.

Figure 4 shows the lattice spacings of PCO and YSZ measured at these conditions parallel to (x) and normal to (y) the interface. Figure 4 also shows the ratio of PCO lattice spacing normalized against the corresponding values for the YSZ substrate located within 15 nm of the PCO-YSZ interface, where we determined the interface position based on image contrast

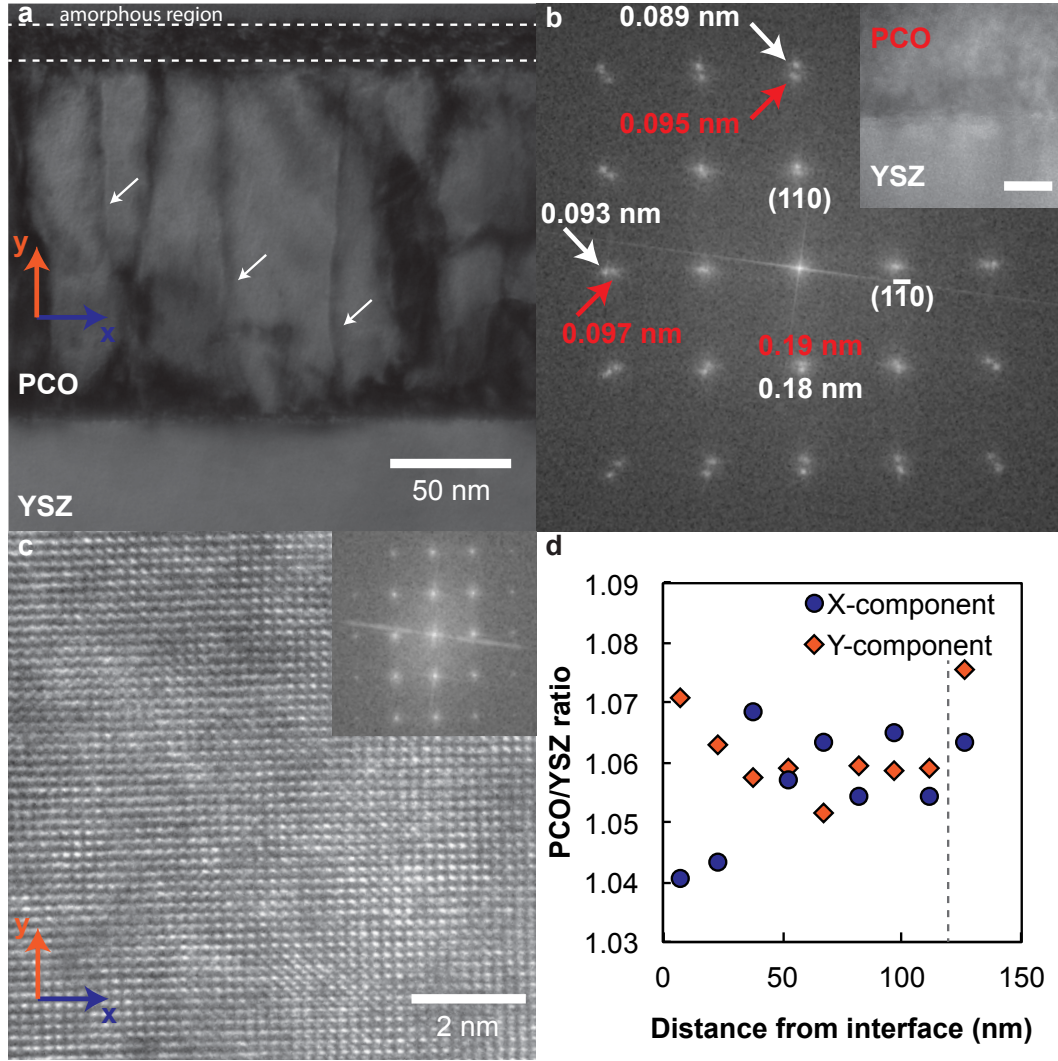


Figure 2: (a) Low magnification image of $\text{Pr}_x\text{Ce}_{1-x}\text{O}_{2-\delta}$ (PCO) film on yttria stabilized zirconia (YSZ) substrate cross-section at room temperature. Threading features propagating from the YSZ interface to the surface are highlighted by white arrows. The focused ion beam preparation resulted in a disordered and reduced "surface layer" separated by dashed lines. (b) Fast Fourier Transform (FFT) of PCO-YSZ interface (inset, 5 nm scale bar) showing doubled reflections indicative of epitaxy. Red arrows denote PCO spots, and white arrows denote YSZ spots. Sample tilt accounts for slight FFT pattern asymmetry. (c) High resolution image of PCO film showing atomic resolution and coordinate system (inset, FFT of this region). Lattice spacing parallel to (x) and normal to (y) the film-substrate interface indicated by blue and orange, respectively. (d) The ratio of PCO lattice spacing to YSZ as a function of distance from the interface, demonstrating expected $\sim 6\%$ mismatch and anisotropic strain within 30 nm of the interface.

associated with defects at the interface discussed in the following section. We note that because we conducted high temperature imaging on a different specimen than the specimen analyzed at room temperature in Fig. 2, with a different FIB-cut orientation and imaging conditions, the lattice spacings observed for Sample A in Fig. 2(b) are not identical to those observed in Fig. 4(a-b). Both the PCO and YSZ crystals exhibited thermal expansion; however, the PCO film also exhibited chemical expansion. This additional capacity of the PCO film to exhibit expansion due to cation valence and oxygen vacancy concentrations that vary with temperature can be recognized through comparison of the "reduced" and "oxidized" lattice spacing ratios. Note that PCO at temperatures $>500^{\circ}\text{C}$ is capable of fast oxygen exchange and is expected to equilibrate to the vacuum (low pO_2) in the TEM column within minutes by releasing oxygen (*i.e.*, undergoing electrochemical reduction).^{35,43} Thus, at 650°C , PCO was reduced significantly within the 15-20 min required to focus the electron probe. However, at a lower temperature of 300°C , comparison of pre-oxidized and pre-reduced samples was possible, allowing direct observation of thermal and chemical expansion.

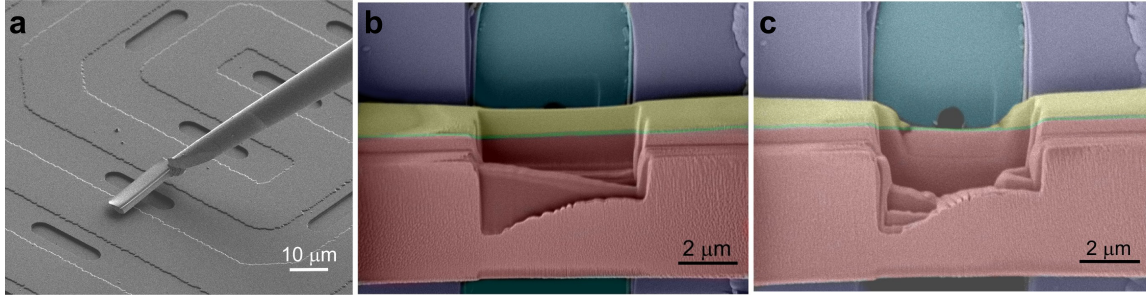


Figure 3: Scanning electron microscope image of a $\text{Pr}_{0.1}\text{Ce}_{0.9}\text{O}_{2-\delta}$ (PCO) on yttria stabilized zirconia (YSZ) cross-section prepared by focused ion beam (FIB) milling. (a) After milling, Sample B was placed on a high temperature heating chip that uses Pt heating elements (spirals) to raise the sample temperature up to 650°C . (b) Higher magnification image with false color shows the different regions of the FIB cross-section placed over a slit in the Si_3N_4 of the heating chip. Colors indicate: YSZ substrate (pink), PCO film (green), Pt capping layer (yellow), Si_3N_4 window (turquoise) and thicker Si_3N_4 (purple). (c) The slit was expanded by FIB-milling into the Si_3N_4 window after cross-section placement.

The EELS spectra in Fig. 5 confirmed the electrochemical reduction of PCO at elevated

temperature. We recorded these spectra at a distance of 10 nm from the interface at each condition. The spectra shown in Fig. 5 exemplify the features used to characterize cation composition and oxidation state. The key features in these images are the Ce M5/M4 peak area ratio (quantified in Fig. 5(b)) and the shape of the Pr M5 peak; the EELS signature of PCO at different oxidation states was characterized previously and reported elsewhere.^{41,44} Pr reduces preferentially to Ce, and when this occurs the Pr M5 peak narrows and shifts to lower energy. This shape change was apparent for the reduced spectra in Fig. 5, including the "post-oxidized" spectrum that we recorded upon heating the oxidized sample to 650°C. We quantified the change in peak shape using the peak full width half maximum (FWHM) reported in Fig. 5(c). The Pr M5 peak width did not change appreciably when we heated the reduced sample from 300 to 650°C. In contrast, the peak narrowed with increased temperature (from 300 to 650°C) for the oxidized sample. Elevated temperature of 650°C should be sufficient to elicit oxygen loss (sample reduction) inside the TEM column. Thus, Pr contained in reduced samples or in samples above the oxygen exchange threshold temperature of $\sim 500^\circ\text{C}$ should be assumed to be chiefly in the +3 state.

The EELS signature for Ce oxidation state, as characterized by a change in the relative heights of the Ce M5 and M4 peaks (and associated areas) can be readily observed in Fig. 5. For Ce, increased M5/M4 ratio and associated left-shifted M5 and M4 peaks (with appropriate peak referencing) indicate $\text{Ce}^{+4} \rightarrow \text{Ce}^{+3}$ cation reduction.⁴⁴ Thus, it is clear that the "reduced" samples in Fig. 4 were reduced to the point of Ce reduction, an effect that was most pronounced for sample reduction at 650°C (orange, dashed line, Fig. 5). Changes in the EELS signature for Pr reduction were quantifiable but less pronounced than those of Ce oxidation. We further note that the "post-oxidized" sample at 650°C did not achieve complete reduction; this suggests that inside the TEM chamber the process of oxygen loss associated with Ce reduction was relatively slow (on the scale of 10-30 min) despite the small sample thickness (<100 nm). Note that we did not ascribe physical interpretation to the apparent peak shifts in Fig. 5, as no standard peaks were available to calibrate spectra

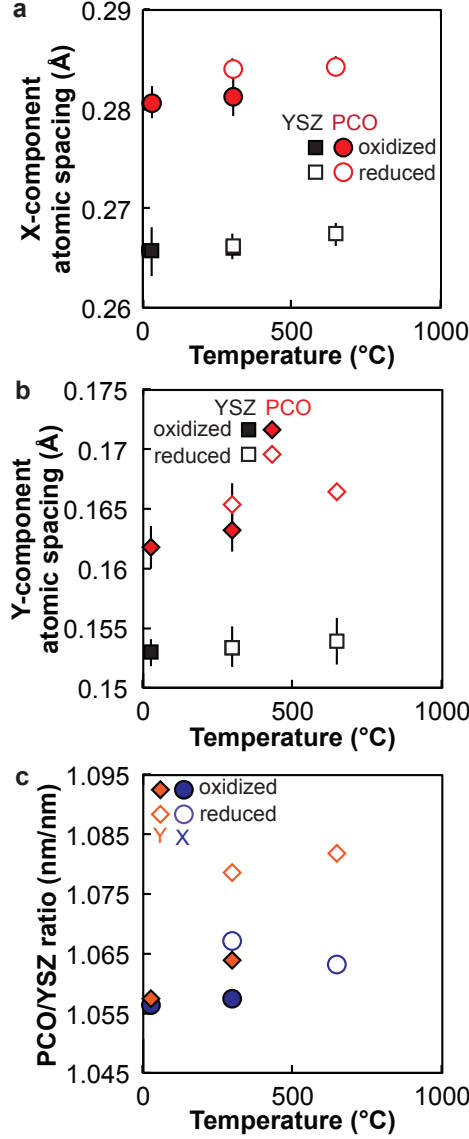


Figure 4: (a) Lattice spacing parallel to the interface (x -component) and (b) normal to the interface (y -component) in $\text{Pr}_x\text{Ce}_{1-x}\text{O}_{2-\delta}$ (PCO) and yttria stabilized zirconia (YSZ) lattices at four conditions of temperature and oxidation state imaged by scanning transmission electron microscopy (STEM). We conducted sample imaging for the electrochemically reduced state of PCO (300°C followed by 650°C), followed by re-oxidation of PCO and imaging (25°C followed by 300°C). We normalized PCO lattice spacing normal to the interface (y -component) with respect to the expected YSZ lattice spacing resulting from thermal expansion, to account for varying tilt angles during different imaging sessions. We determined the y -component lattice spacing from the out-of-plane diffraction spots produced by the hexagonal fast Fourier transform (FFT) diffraction patterns from the STEM images. This hexagonal FFT pattern also means that the x and y component lattice spacings differ in magnitude. PCO lattice spacings reported as mean and standard deviation measured at multiple locations within 10 nm of the interface. (c) Ratios of PCO lattice spacing normalized by YSZ lattice spacing in the same conditions.

recorded at different times and under distinct *in situ* conditions.

Figure 4(c) illustrates that the strain variation with distance from the film-substrate interface that we observed in the as-grown film at room temperature (Fig. 2(d), Sample A) was absent upon re-oxidation of PCO at high temperature (Sample B). As described in the Experimental section, Sample B was subjected to elevated temperatures of up to 650°C for extended times, in effect annealing the sample prior to high temperature STEM imaging. This contrast in the magnitude of strain within 10 nm of the film-substrate interface in the as-prepared and post-annealed specimens at room temperature suggests that the annealing process relieved interfacial stress sufficiently to relax the film lattice upon re-oxidation at elevated temperature. If we refer to the distinct PCO lattice spacing in the x and y directions as "strain anisotropy," then Fig. 4 shows that such strain anisotropy was evident for all conditions except PCO oxidized at room temperature. Thermal expansion in PCO and YSZ was comparable (about 30% larger for PCO^{45,46}) such that PCO lattice strain (relative to YSZ) parallel to the interface changed minimally under conditions allowing only thermal expansion. Even so, PCO expansion normal to the interface (y -component) increased slightly with increased temperature for the oxidized or reduced cases. In contrast, chemical expansion affected strain both along and normal to the interface (both x and y -components) though strain normal to the interface was modulated more strongly. At 300°C, PCO in the reduced state exhibited out-of-plane strain (strain in the y -direction) of 1.4% as referenced to the oxidized state, whereas in-plane strain along the interface (strain in the x -direction) was only 0.9% upon reduction. We estimate the measurement error for strain along the interface as $\pm 0.15\%$, given that this in-plane strain was 0.6% for PCO reduced at 650°C. Even with this level of measurement uncertainty, the strain normal to the interface was $\sim 50\%$ greater than that parallel to the interface, indicating clearly that chemical expansion resulted chiefly in increased atomic spacing normal to the interface (and therefore increased film thickness) due to the film-substrate interface constraint. As measurable expansion was also quantified parallel to the interface, we assert that the chemical expansion coefficient can be understood

to be both *thickness-dependent* and *spatially anisotropic* with respect to distance from the interface.

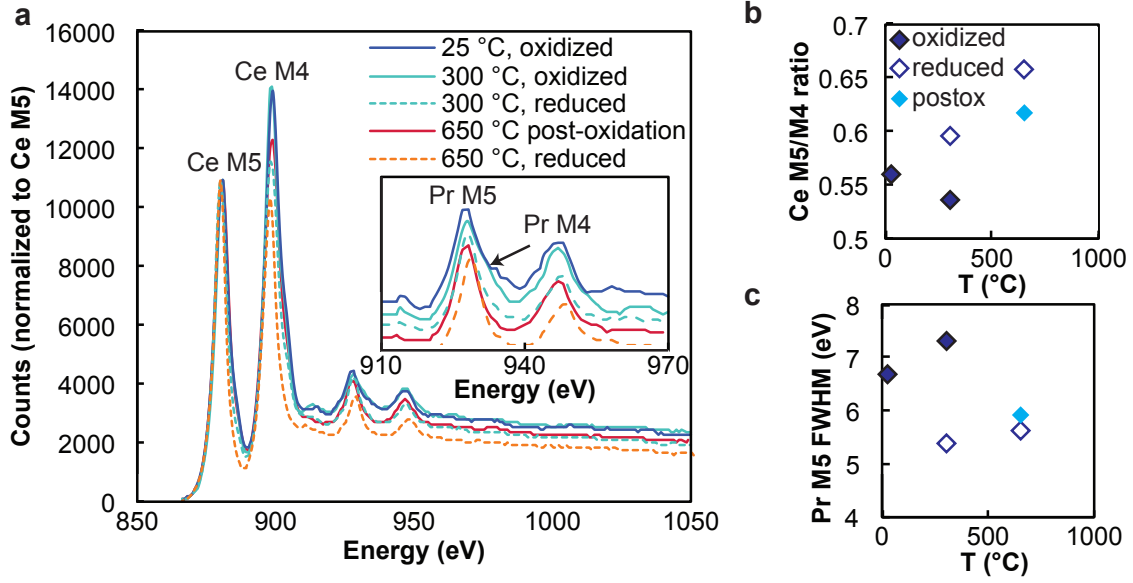


Figure 5: (a) Electron energy loss spectra at several imaging conditions of temperature and oxidation state. These spectra were shifted against the Ce satellite peak at 1163 eV which is not necessarily an immovable reference, and were collected at a distance of 10 nm from the yttria stabilized zirconia interface. Inset shows Pr M5 and M4 peaks after separate Pr background subtraction. (b) Increased Ce M5/M4 peak area ratio with increased temperature or prior sample reduction indicative of increased Ce^{+3} concentration. Additionally, the Pr M5 peak (highlighted by the black arrow) narrowed with Pr cation reduction. (c) The full width half maximum (FWHM) of the Pr M5 peak decreased as Pr reduced.

By considering Fig. 4 and the chemical expansion coefficient of PCO, we can infer differences in point defect concentration, as quantified by the change in non-stoichiometric parameter $\Delta\delta$ that existed in the PCO films in the oxidized and reduced states *in situ*. Using the strain parallel to the film-substrate interface resulting from reduction of PCO at 300°C, $\Delta\delta$ is approximately 0.1 according to Eq. 2. Taking account of the strain measured for the reduced sample at 650°C, this estimate of $\Delta\delta$ is 0.06-0.1. Assuming that mechanical constraint of the substrate amplified the film strain normal to the interface (*y*-component) by approximately a factor of two,²⁰ we can also estimate $\Delta\delta$ independently at 0.08. Since we observed measurable and repeatable strain parallel to the film-substrate interface, a slightly larger value of $\Delta\delta$ of about 0.1 appears plausible. Given that these films have a

Pr concentration of $x = 0.1$, the reduction of Pr can contribute a change in δ of only 0.05. Therefore, the remaining strain must be attributed to that arising from Ce reduction, an assertion that is further supported by our EELS data in Fig. 5. Given these results, we infer that either the effective partial pressure of oxygen pO_2 within the TEM chamber was $< 10^{-18}$ atm (the point of Ce reduction in PCO at 650°C ^{14,47}), and/or the reduced PCO film cross-section was significantly more reduced than expected based on available defect models. Since the TEM vacuum was at about 10^{-11} atm for the results reported herein, a reducing gaseous species such as H_2 or CO would need to have been present to achieve such a low pO_2 , which seems unlikely. The electron beam dosage may have induced some reduction of PCO, but we intentionally varied the imaging location to minimize such effects, and similar beam dosages applied to oxidized samples did not cause detectable Pr or Ce reduction (see Fig. 5). Therefore, we attribute the observed lattice expansion to a combination of low pO_2 ($< 10^{-12}$ atm) and enhanced sample reduction in these very thin (< 100 nm) PCO cross-sections.

Interface structure

The variation of chemical expansion exhibited by the PCO films as a function of orientation with respect to the film-substrate interface results from the mechanical constraint of the interface. We conducted an annealing study of the PCO-YSZ interface upon initial heating to 650°C inside of the TEM (Sample B; see Experimental and SI Fig. S8). Figure 6 shows that periodic image contrast features existed normal to and near (if not transecting) the interface during this initial heating study, of spacing $\lambda \sim 4$ nm. These features resulted from lattice distortion around misfit dislocations that caused diffraction-based contrast variation in the image in the region of disorder. During sample annealing, the sample lattice resolved more clearly and inclusions with dissimilar orientation realigned with the rest of the PCO lattice.

When we subsequently imaged the same sample by STEM, the interface continued to exhibit a periodic array of defects, as shown in Figs. 7(a) and (c). Geometric phase analysis

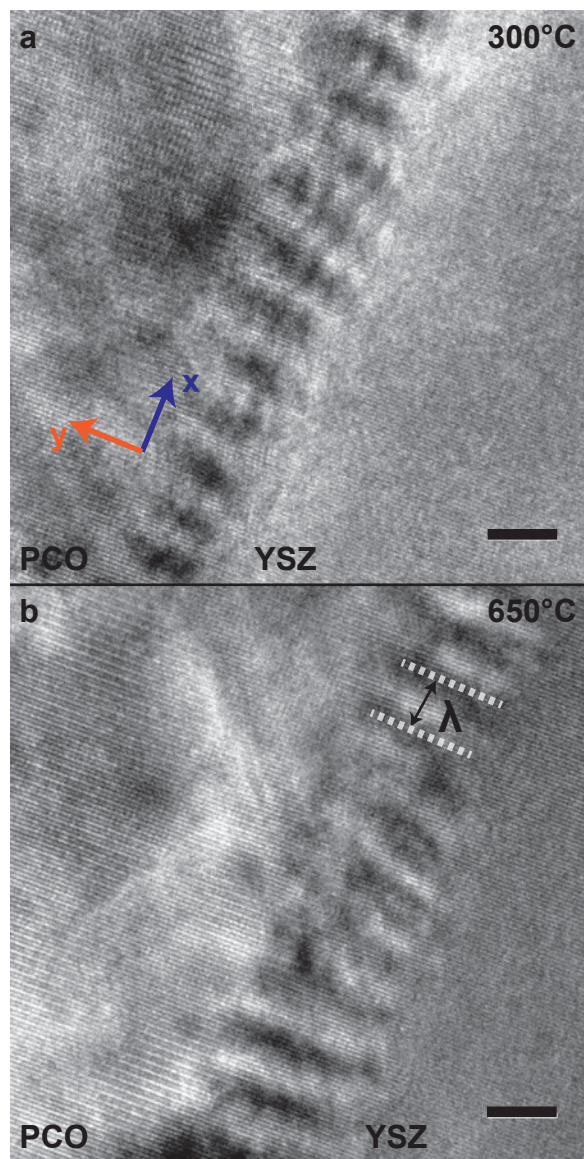


Figure 6: Phase contrast transmission electron microscope images at the same resolution of the PCO-YSZ interface at (a) 300°C and (b) 650°C and at different locations showed interfacial contrast fringes. Interfringe spacing λ marked in (b) is ~ 4 nm, agreeing well with edge dislocation spacing determined based on scanning transmission electron microscopy images. Further analysis of interfacial contrast is available in Supporting Information. Scale bars are 5 nm.

(GPA) of these images produced strain maps such as those shown in Figs. 7(b) and (d), indicating periodic hourglass-shaped strain features along the interface with a characteristic spacing of ~ 4 nm. This spacing agrees well with that of λ identified for the series of images included in Fig. 6, and the strain profiles in the GPA images are consistent with GPA contrast expected of edge dislocations. High resolution imaging of these interfacial defects (Fig. 7(e)) also indicated a mismatched lattice at this interface, and inverse Fourier transform analysis resolved the position of an apparent extra lattice half-plane (Fig. 7(f), arrow).

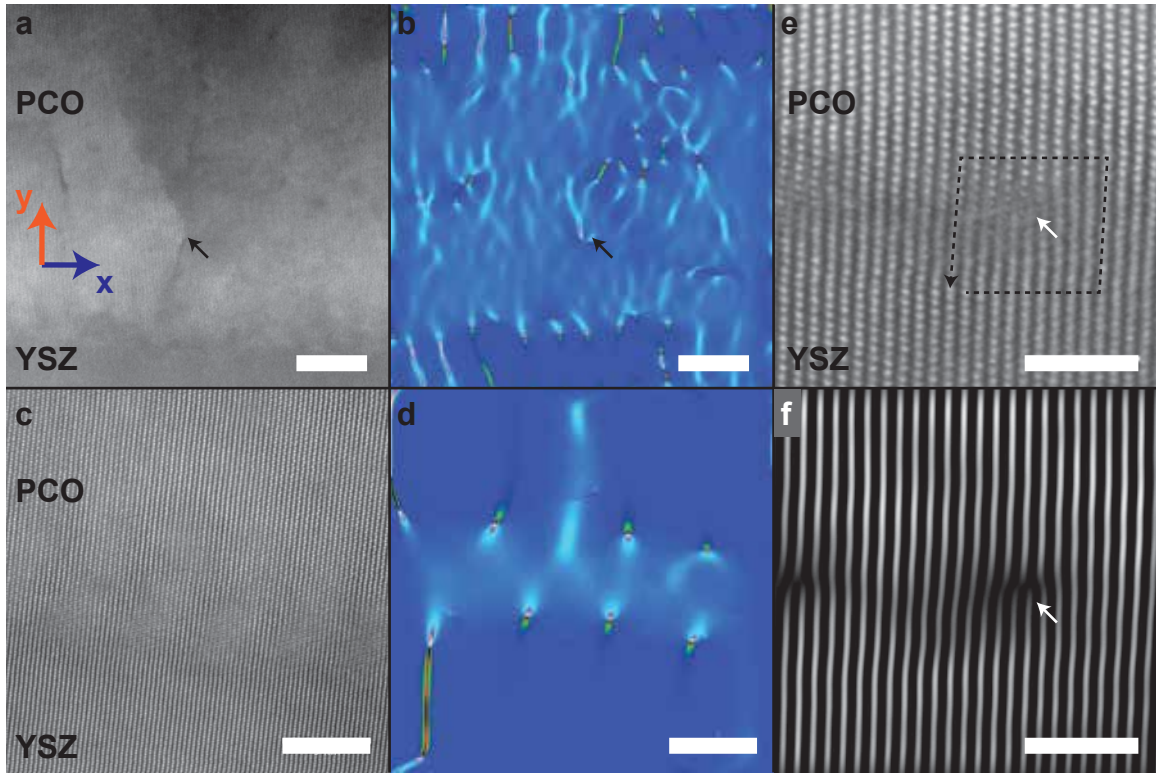


Figure 7: (a) Scanning transmission electron microscope (STEM) image of pre-oxidized $\text{Pr}_x\text{Ce}_{1-x}\text{O}_{2-\delta}$ (PCO)- yttria stabilized zirconia (YSZ) interface with a threading defect at room temperature. (b) Geometric phase analysis of (a) showing interfacial periodic strain field and threading linear defect (indicated by black arrow). Scale bars for (a) and (b) are 10 nm. (c) STEM image of fully reduced PCO-YSZ interface at 300°C and (d) corresponding geometric phase analysis. The distance between strain-field cores is 4.1 and 4.3 nm in (b) and (d), respectively. Scale bars for (c) and (d) are 5 nm. (e) High resolution image of a misfit dislocation at the PCO-YSZ interface at room temperature with Burgers circuit drawn (black, dashed line); (f) inverse Fourier transform analysis of this defect highlighting the position of the extra half plane of atoms (white arrow). The distance between dislocation cores in this image is 4.3 nm. Scale bars for (e) and (f) are 2 nm.

Several previous TEM studies have reported observation of edge dislocations at the interface between epitaxial ceria (both undoped and Sm-doped) and YSZ substrates.^{24,36,37} Generally imaged at room temperature, these dislocations were present in both oxidized and highly reduced films for which sample reduction (even to an ordered structure with $\delta = 0.3$) was induced by high energy irradiation with the electron beam.^{20,24,36} The spacing of CeO₂-YSZ misfit dislocations reported previously for the (100) orientation ranges from 3.7-4.8 nm, and is understood generally to relieve misfit stress at the interface.^{20,36,37} In molecular dynamics simulations of CeO₂ recrystallization from an amorphous phase adjacent to crystalline YSZ, arrays of misfit edge dislocations appeared spontaneously, along with other mixed screw-edge dislocations that extended into the film.⁴⁸ Sheth *et al.* also observed by TEM the existence of threading dislocations for PCO films grown on YSZ.²⁰

Periodic contrast fringes similar to those in Fig. 6 have been observed by TEM in interfaces such as heteroepitaxial GaSb/GaAs and grain boundaries in Bi_{0.5}Sb_{1.5}Te₃.^{49–51} In prior work, those features were attributed by the authors as resulting from periodic arrays of misfit dislocations. In our own images, the disordered nature of the lattice in this interfacial region precluded direct, lattice-resolved observation of these features during the initial annealing cycle, although later analysis *via* STEM showed stress and lattice features consistent with edge dislocations with comparable interfringe periodic spacing λ . Upon considering and eliminating other possible sources of periodic contrast at the interface (see discussion of Figs. S1-4 in Supporting Information, SI), we conclude that the periodic contrast and the periodic line defects observed by TEM and STEM, respectively, were both due to misfit dislocations and associated strain fields. We also note that during sample annealing, both the interfringe periodic spacing λ and the width of these contrast features evolved as a function of temperature, pointing to possible stress relief during chemical expansion at the highest temperatures. Further discussion of those observations can be found in the SI (Figs. S1-4).

After this annealing process, we also imaged and analyzed the PCO-YSZ interface *via* STEM with EELS to consider measurable features of space charge and cation segregation at

the interface. We observed no evidence of cation segregation, and, although expected based on previous observations of epitaxial CeO_2 -YSZ interfaces,²⁴ we found limited evidence of space charge in our own samples. For the oxidized film at 300°C, we resolved an apparent increase in the Pr^{+3} concentration at the PCO-YSZ interface, possibly indicating space charge. However, we identified no such trend for Ce^{+3} in highly reduced samples. Supporting Fig. S5 provides the EELS spectra for this result, along with additional discussion in SI.

Taken together, we conclude that the PCO films grown on YSZ exhibited periodic arrays of dislocations that exerted strain fields identifiable from both TEM and STEM images. At sufficiently high temperatures and at chemical-expansion induced stresses, these defects appeared mobile enough to partially relieve interfacial stress, as discussed further in Supporting Information. Upon sample cooling and re-oxidation, those defect features remained immobile in position and some Pr^{+3} enrichment appeared at the PCO-YSZ interface accompanied by emergence of longer range, threading defects.

Threading defects

After sample re-oxidation (see Experimental and Supporting Fig. S8 for flow chart of experimental procedures), we observed by STEM defects extending from the film-substrate interface that were not visible previously. Figures 7(a) and 8 show one such defect, along with an EELS map of the associated Ce M5/M4 peak area ratio. The EELS map exhibited a maximum at the position of the linear defect, shown also in the inset to Fig. 8(a). Figure 8(c) compares spectra within and far from the defect. We detected this signature, which indicates increased sample reduction at the position of the defect, to a lesser degree for the same defect at room temperature (SI Fig. S6), and also for a similar defect imaged for the oxidized sample at 300°C (SI Fig. S7). We consistently observed sample reduction relative to the lattice at these defects, both at low temperature, oxidized conditions (when the rest of the sample should contain minimal Pr^{+3} , or Ce^{+3} content) and at high temperature, reduced conditions. This localized reduction implies that these defects acted as traps

for reduced cations and/or oxygen vacancies relative to the rest of the lattice, establishing spatial heterogeneity of such defects within the lattice.

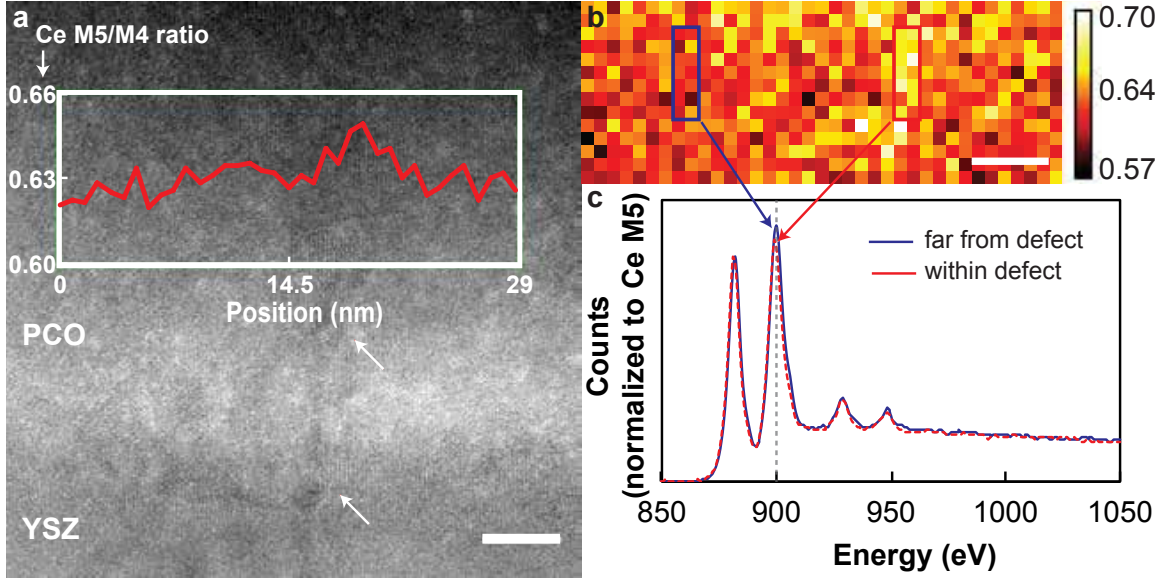


Figure 8: (a) ADF-STEM image of a linear defect (white arrows) propagating from the PCO-YSZ interface through the PCO film at 650°C toward the PCO free surface with selection region for EELS data collection highlighted. The plot shows the average Ce M5/M4 ratio moving left to right across selection region, showing a maximum at the linear defect. (b) Map of the Ce M5/M4 EELS peak area ratio from the highlighted region in (a). (c) A comparison of EELS spectra within and outside the linear defect confirmed Ce reduction inside the defect through both changing peak height and peak shift. Scale bars are 5 nm.

Linear defects that appeared in re-oxidized (redox cycled) samples thus may have acted as sinks for Ce^{+3} cations, and possibly also for corresponding oxygen vacancies. Because the cation oxidation state change requires only small polaron hopping, oxygen vacancy diffusion (and associated volume change) could be a mechanism of stress relief during re-oxidation at 650°C. Not only should reduced cations correlate with increased sample volume (which is difficult to resolve given the disordered nature of these regions), but they would also potentially affect charge transport and gas reactivity properties.^{42,52} For example, Sun *et al.* determined that edge dislocations in CeO_2 could cause charged defect localization of both reduced cations and oxygen vacancies within the tensile and compressive strain fields around the dislocation. The association between these charged defects could then trap further ion motion, potentially impeding oxide ion conductivity.⁴² While the exact classification of the

defects imaged in Figs. 8, S6, and S7 could not be identified, the general result of Sun *et al.* is likely still applicable. This threading defect, which trapped an enriched concentration of reduced cations, would likely also act as a barrier to oxygen vacancy diffusion. While the relatively degraded lattice resolution within the defect precluded measurement of lattice spacing, such image quality in that region also suggested a high degree of disorder such as might be expected from a relatively large concentration of oxygen vacancies. It is also possible that this was actually a space-charge region, in which case a large concentration of reduced cations surrounding an oxygen-vacancy-enriched core should correspond to increased lattice parameter.^{17,23}

Appearance of such defects in redox cycled, mechanically constrained films could explain several observed differences between film and bulk PCO *in situ*, including enhanced oxygen vacancy concentrations,³⁵ relatively lower elastic modulus than expected for defect models of bulk PCO, and a high degree of variability in the measured Young’s modulus by nanoindentation.¹⁶ Space charge regions of reduced cations distributed inhomogeneously throughout a film would be expected to have larger volume than the surrounding lattice, causing associated, inhomogeneous decreases in elastic modulus. Furthermore, there is the potential that propagation of such defects to the film free surface could catalyze oxygen vacancy formation, even as it could impede charge transport.^{42,52} These defects appeared in our samples after re-oxidation that corresponded to a change in stress state (in the tensile direction); if this is a general effect in other non-stoichiometric oxides, this mechanism could also mediate effects of tensile strain on oxygen exchange reactivity and diffusivity.

Dynamic imaging of *in situ* oxygen breathing

We conclude our discussion with direct observation of PCO expanding during *in situ* re-reduction at 650°C. After oxidizing the PCO film outside the TEM column, we inserted the sample into the microscope and recorded images as PCO equilibrated by releasing oxygen into the TEM vacuum (see Experimental and Fig. S8). While others reduced CeO₂ *in*

situ by electron-beam irradiation previously,^{36,53} those studies did not analyze in detail the anisotropic or localized chemical expansion during the re-oxidation process. After focusing on a fully oxidized film at room temperature and 200°C, we rapidly heated the film (within 2 minutes) to 650°C inside the TEM column. We then collected a time series of images such as the one shown in Fig. 9(a) while the sample reduced (and underwent chemical expansion) inside the TEM vacuum. We collected images of many regions in the PCO film in order to prevent any sample reduction *in situ* by the electron beam. As shown in Fig. 9, for each image we analyzed two regions: one adjacent to the interface, and one far (>20 nm) from the interface. These images exhibited two characteristic types of fast Fourier transform (FFT): a hexagonal (72°, Fig. 9(b)) pattern and a rectangular (90°, Fig. 9(c)) pattern. These patterns sometimes coexisted within an analyzed image, indicating slightly different lattice projections as dominant features in different parts of the film during re-reduction. We observed no such lattice variability in the previously discussed STEM images for either oxidized or reduced samples, suggesting that the redox process may have involved some local nucleation phenomena or lattice distortion. It is also possible that these small grains nucleated near and were constrained by residual amorphous surface layers of the TEM cross-section during annealing.

We reported the lattice spacing both parallel to the interface (x) and normal to the interface (y) based on the FFT patterns as a function of time in Figs. 9(d)-(e). Both data sets showed a positive slope with time, reflecting lattice dilation as the sample actively released oxygen from its structure. We were able to resolve the x -component lattice planes more easily than the y -component planes, and also more consistently between the two lattice projections. This enabled a statistical analysis of the linear fits applied to the x -component data. This analysis produced 95% confidence intervals (CI) for the intercept and slope of the linear fit (Fig. 9 shaded regions), from which we determined that the mean PCO lattice spacing along the direction parallel to the interface (x) was smaller near the interface (0.277 nm) as compared to that located more than 20 nm from the interface (0.279 nm). We did

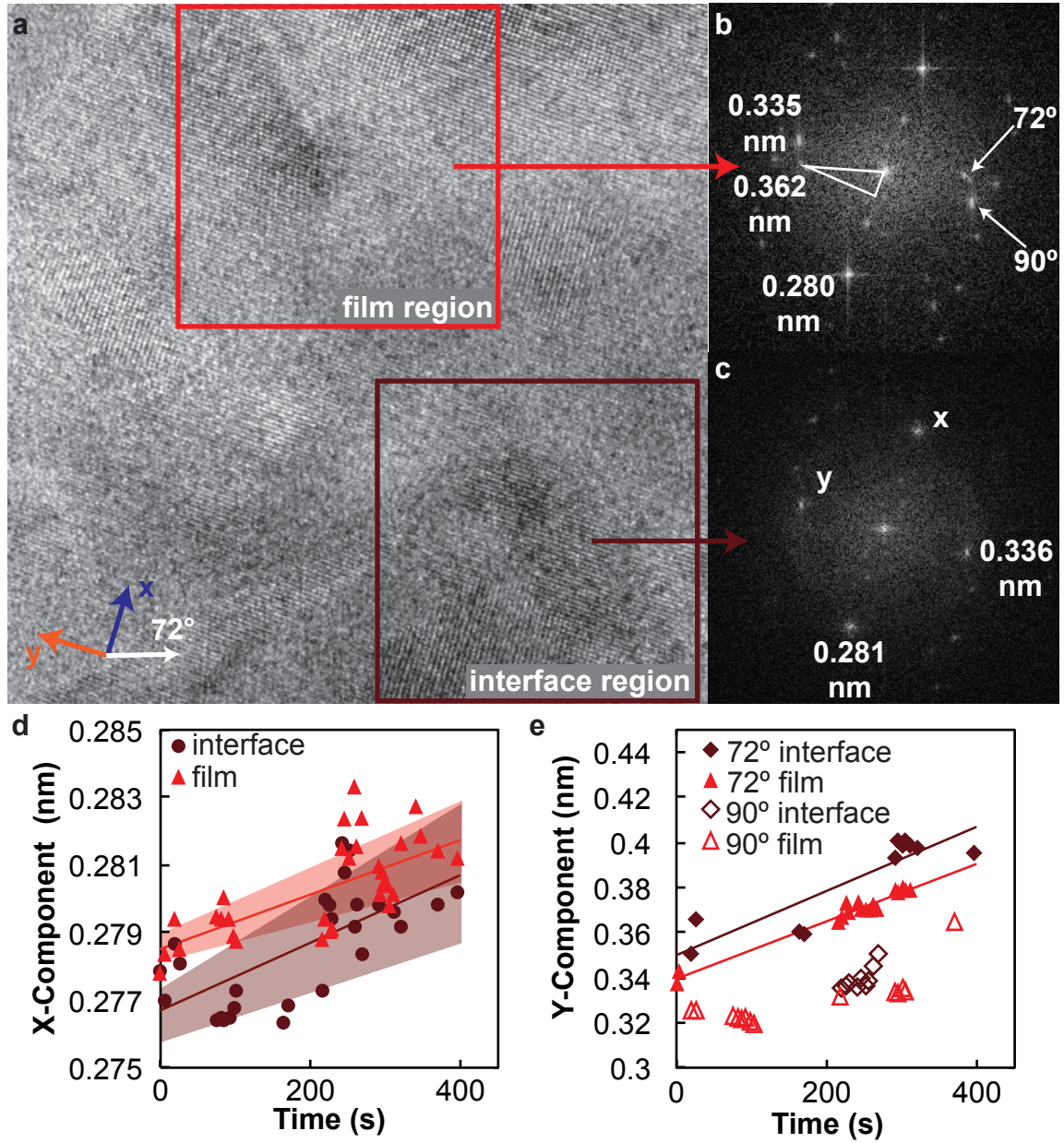


Figure 9: (a) Example TEM image from time series collected during sample reduction *in situ*, showing regions selected near and far from the PCO-YSZ interface for lattice spacing analysis. (b) FFT resulting from the film region with the 72° and 90° y -component (normal to the interface) lattice reflections highlighted by white arrows. (c) FFT from the interface region in (a). (d) Measured x -component (parallel to the interface, with shaded 95% confidence intervals for the linear fit) and (e) y -component lattice spacing *vs.* time as the cross-section equilibrated with the TEM vacuum (*i.e.*, reduced).

not find the differences in slope to be statistically significant, in that the 95% CIs for the slopes of the linear fits overlapped. However, these data are consistent with the concept that the region nearest the interface existed in a state of compression relative to the bulk, prior to chemical expansion. We further found that this relative (though statistically insignificant) difference in x -component lattice parameter near and far from the interface was also retained during film expansion.

The PCO film also exhibited positive strain with time in the direction normal to the interface, which was larger for the region closest to the interface. The overall apparent slope of this lattice strain direction with time was statistically larger than that observed for the strain parallel to the interface, indicating (consistent with Fig. 4(c)) that chemical expansion was more pronounced in the direction normal to interface (y) than parallel to the interface (x). However, we note that the y -component data in Fig. 9(e) are too sparse, with too large of an uncertainty range, to identify statistical differences between the interface and film regions for the intercepts or slopes. This spatially inhomogeneous strain also could not be attributed unambiguously to phase separation or ordering (see SI). The time series images therefore demonstrated the PCO exhibiting spatially anisotropic chemical expansion *in situ* as the structure breathed oxygen out of the lattice.

Conclusions

We reported *in situ* TEM, STEM, and EELS analysis of chemical expansion in the model non-stoichiometric oxide thin film $\text{Pr}_{0.1}\text{Ce}_{0.9}\text{O}_{2-\delta}$ (PCO) grown on yttria stabilized zirconia (YSZ) substrates. We found that such PCO films exhibited anisotropic chemical expansion that was more pronounced in the direction normal to the interface (y -component) relative to the direction parallel to the film-substrate interface (x -component). This lattice expansion also varied with distance from the interface: local strain parallel to the interface was smaller near to the interface, and the reverse was true for strain normal to the interface. PCO

films exhibited periodic arrays of strain fields imaged by ADF-STEM, consistent with misfit dislocation features, that changed size during thermochemical expansion. Upon sample re-oxidation, threading defects appeared in the PCO cross-sections. These defects trapped reduced cations for both oxidized, low temperature conditions and reduced, high temperature conditions, possibly impeding charge transport or affecting local oxygen vacancy formation energies. Finally, we directly observed the PCO film undergoing chemical expansion as it released oxygen, dynamically imaging this anisotropic, position-dependent chemical expansion *in situ*.

These results demonstrated several mechanisms facilitating chemical expansion in thin film non-stoichiometric oxides, including strain anisotropy, long range defect formation, and spatially inhomogeneous strain and composition. Films can be expected to exhibit significant strain normal to the film-substrate interface that may be enhanced for structures that are also thin in the orthogonal dimension, such as the cross-sections considered in this study. The observed anisotropic chemical expansion and lattice strain showed that interfacial stress persists *in situ*. This direction-dependent chemical strain could also impact chemomechanically coupled, volume-averaged properties such as elastic moduli or oxide ion diffusivity. Furthermore, threading defects that appear during redox cycling may localize charged cations *in situ*, potentially impacting total oxygen vacancy content, lattice stiffness, and transport properties. These results provide a direct and detailed analysis of chemical expansion in a thin film non-stoichiometric oxide that will inform the design of high temperature oxide actuators or strain-engineered functional oxides for applications involving gas exchange, storage, or ionic conductivity.

Experimental

Sample preparation

$\text{Pr}_{0.1}\text{Ce}_{0.9}\text{O}_{2-\delta}$ (PCO) films were prepared by pulsed laser deposition (PLD) from oxide targets. The films were deposited onto (001)-oriented single crystal YSZ (8 mol% Y_2O_3 stabilized zirconia) substrates ($10 \times 10 \times 0.5 \text{ mm}^3$; MTI Corporation, Richmond, CA). The 2.5 cm diameter oxide target was fabricated from PCO powders prepared through a Pechini-based gel process described briefly below.⁵⁴ The following starting materials were utilized: cerium (III) nitrate hexahydrate, 99.99% (Sigma Aldrich), praseodymium (III) nitrate hydrate, 99.9%, ethylene glycol (Alfa Aesar) and anhydrous citric acid (Fisher Scientific). Citric acid and ethylene glycol were mixed with aqueous solutions of $\text{Ce}(\text{NO}_3)_3$ and $\text{Pr}(\text{NO}_3)_3$ at 80°C until polyesterification resulted in the formation of a gel. After drying in an oven at 110°C , the as-obtained powder was fired at 450°C for 4 hours and then at 700°C for 3 hours in flowing air. The PCO powders were examined by X-ray diffraction (Rigaku H3R Cu-source Powder Diffractometer) and were found to have a single phase fluorite structure. Dense PLD targets were then prepared by isostatic pressing of PCO powder followed by sintering at $>1400^\circ\text{C}$.

The PLD system (Neocera Inc., Beltsville, MD) was operated with a KrF excimer laser (Coherent COMPex Pro 205) emitting at 248 nm, with 400 mJ/pulse and repetition rate of 8 Hz. The substrates were heated to 600°C during deposition, while the oxygen pressure was maintained at 10 mTorr after pumping the background pressure to less than 8.56×10^{-6} Torr. The film was deposited with 45000 shots after 2000 pre-ablation shots with a substrate to target distance set to 7 cm. Following deposition and prior to cooling, the oxygen pressure in the chamber was increased to approximately 6-7 Torr to facilitate complete oxidation of the film. Film thickness was determined to be 196 nm *via* surface profilometry (KLA-Tencor P-16+ stylus profiler) of the film deposition edge.

Two PCO-YSZ cross-sectional test specimens of final cross-section thickness 50-100 nm

were prepared by focused ion beam (FIB) milling using a Zeiss Crossbeam 540 instrument fitted with an Omniprobe 400 micromanipulator. Samples were transferred from a bulk specimen to windowed test points on a DENS chip. A thin layer of Pt was deposited over the target area using the electron beam (2nA beam current at 5kV for approximately 60s) prior to any ion beam exposure. After this, a standard *in situ* procedure was adopted for liftout.⁵⁵ Initial setup began with a deposition of Pt measuring $20 \times 2 \times 1.5 \mu\text{m}$ using the Ga^+ ion beam, followed by coarse milling steps using a 30kV:30nA beam to remove the bulk of material. The sample was further thinned to a thickness of $\sim 1.5 \mu\text{m}$ using a beam current of 30 kV:1.5 nA and then undercut in preparation for release and lifting out. Throughout the text, samples imaged at room temperature and at elevated temperature are referred to as Sample A and B, respectively.

Liftout was carried out by welding the specimen to an Omniprobe needle using Pt, released with a FIB cut and then lifted out with the stage at 0° tilt. Once clear of the bulk material, the micromanipulator needle was rotated by 90° to present the specimen to the imaging chip. For Sample B, this was in the geometry shown in the scanning electron microscope (SEM) image in Fig. 3(a). The sample was then secured on the chip with ion beam deposited Pt. The chip was then re-orientated for thinning of the lamella and, for high temperature imaging, milling of a window into the nitride membrane. Further thinning was performed at 30kV and 300pA, until the Pt appeared transparent in a 8 kV SE image,⁵⁶ indicating a thickness of $\sim 120 \text{ nm}$. Final polishing was conducted at a reduced voltage of 2 kV to further thin and minimize the amount of damage and reduce levels of implanted Ga in the final specimen to final electron transparency at 5 kV electron energy.

Figure 3(a-c) shows Sample B attached to a heating chip, including false coloring to denote different materials both before and after additional milling to extend the slit in the Si_3N_4 for improved image resolution.

Imaging and EELS

Three microscopes were used to acquire images and spectroscopic analysis described below. Initial room temperature imaging of as-grown PCO films on YSZ (Sample A) was conducted using an aberration corrected JEOL JEM-2200MCO field emission gun TEM/STEM operated at 200 keV, equipped with CEOS image/probe correctors. *In situ* imaging at high temperatures up to 650°C was conducted using a commercially available *in situ* heating holder from DENS Solutions (SH30-4M-FS). The resistance of the platinum coil in the heating chip (DENS Solutions DENS-C-30) is monitored in a four-point configuration, and the temperature is calculated using the Callendar-Van Dusen equation (with calibration constants provided by the manufacturer). Slits were produced into the Si₃N₄ membrane by FIB milling. Phase contrast transmission electron microscopy of samples at elevated temperatures was conducted with a standard JEM-2100 (JEOL) transmission electron microscope operated at 200 kV, with a LaB₆ filament, while both high temperature and room temperature annular dark field - scanning transmission electron microscopy (ADF-STEM) of Sample B was conducted using a JEOL ARM-200F microscope operated at 200 kV.

Thermal and chemical expansion of the PCO film in Sample B were induced, respectively, by controlling film temperature (using the DENS *in situ* heating chip) or changing the oxidation state of the PCO film by high temperature annealing in either oxidizing (air) or reducing (TEM vacuum $<10^{-11}$ atm) environments. While both PCO and YSZ were expected to respond to changes in temperature with thermal expansion (increased lattice parameter with increased temperature), high temperature annealing in oxidizing or reducing environments was only expected to induce chemical expansion in PCO, because YSZ is not expected to be active to oxygen exchange. Because PCO undergoes oxygen exchange above 500°C, it was also possible to trap PCO films in an oxidized or reduced state by rapidly cooling samples below the 500°C threshold after annealing. For PCO, oxygen loss and associated cation reduction (caused by annealing at high temperature inside the TEM vacuum) should result in increased lattice parameter due to chemical expansion. The data

presented in Figs. 4-9 are the result of a series of experiments described below and presented in the form of a flow chart in Supporting Fig. S8. Fig. S8 also illustrates schematically how changes in control variables (*e.g.*, T or oxidation state) should change lattice parameters in PCO and YSZ, respectively.

An initial annealing study was conducted using the JEM-2100 while heating Sample B from room temperature to a maximum temperature of 650°C in increments of 50-100°C and imaging along the film and interface cross-section. This resulted in substantial electrochemical reduction of PCO while inside the TEM column at $T > 500^\circ\text{C}$. The sample was rapidly cooled to room temperature to maintain this reduced state and then imaged and analyzed *via* EELS using the ARM-200F microscope at 300°C and 650°C. Sample B was then heated to 650°C for 30 min outside of the TEM column to enable re-oxidation of the PCO film. To observe sample reduction *in situ*, Sample B was cooled rapidly to room temperature and heated to 200°C with image focusing adjustments at each temperature, before rapidly heating the sample to 650°C within 2 min inside the JEM2100. For the next 7 min, sample equilibration to the column vacuum was observed by continuous imaging along the film near the interface; images were recorded every 10-30 sec, with the imaging location translated every 0.5-2 min. The sample was then re-oxidized again at 650°C in air and placed in the ARM200 at room temperature. Imaging and EELS analysis were conducted at room temperature, followed by 300°C (a temperature sufficient to prevent significant oxygen loss despite the TEM vacuum), followed by 650°C. This last condition following intentional oxidation of the PCO is labeled "post-oxidation" or "postox" in the figures, to distinguish from image acquisition at 650°C prior to forced oxidation. The sequence of experiments is illustrated in Supporting Fig. S8, which also lists which figures draw data from which experiments.

EELS data were gathered using the ARM-200F microscope for an energy range of 300-2350 eV. To mitigate sample reduction by electron beam dosage, the imaging location was frequently adjusted for all imaging conditions. However, little evidence of beam-induced sample reduction was observed during imaging, due to the larger cross-section thickness

compared to the reports of Sinclair *et al.*³⁶

Data analysis

Images were analyzed using Digital Micrograph version 3. To determine lattice spacing in PCO and YSZ, Fast Fourier transforms (FFT) of TEM and STEM images were analyzed for peak positions using the Measure Spacings and Angles script in the DiffTools package available from D.R.G. Mitchell.⁵⁷

Images above reference the x - y plane as the imaged cross-section plane of the PCO lattice, with the image z -axis oriented along columns of atoms extending into the milled cross-section. We thus refer to the displacements normal to the film-substrate interface as "out-of-plane" and select a y -axis orientation normal to the interface. Thus, displacements normal to the film-substrate interface are denoted as those extending in the y -direction normal to the interface, or "out-of-plane" because such displacements would indeed represent film thickness increased or decreased in a direction perpendicular to the film plane and free surface of the film in plan view (*i.e.*, rotated 90° from the cross-sectional view of the TEM image plane). Displacements parallel to the interface are denoted as those observed in the x -direction, or "in-plane." Clearly, the z -axis in this orthogonal axis set is normal to the cross-section surface, and any misorientation of the lattice displacements with respect to the x - y axes refer to those offset from the film-substrate interface normal.

To determine the x - and y - components of PCO lattice spacing for ADF-STEM data at each condition, four to eight square regions of 10×10 nm were selected adjacent to the interface, and the FFT peak positions and angles were measured. Because FFT representations of the ADF-STEM images produced a hexagonal pattern as shown in Fig. S9, the y -direction projection of the out-of-plane spots ($\theta \sim 72^\circ$) were used to determine the "y-component" lattice spacing normal to the interface. The resulting magnitudes of x - and y - component spacing were averaged for each condition and compared to the spacings measured in the same imaging conditions for the YSZ substrate. In the case of rectangular lattice projections

(Sample A room temperature images and parts of Sample B images used for Fig. 9), this analysis did not require the additional step of accounting for angles θ . Strain maps were produced by Geometric Phase Analysis (GPA) of x -component or in-plane strain parallel to the film-substrate interface, using the FRWRTools plugin for Digital Micrograph written by C. Koch.³³ The following parameters were used for GPA: 3 nm resolution, 1 nm smoothing.

Observed strains were computed with reference to the YSZ sample, specifically by determining the ratio of PCO lattice spacing to YSZ lattice spacing at the same imaging condition (T , oxidized or reduced sample) for each FFT peak of interest, and then comparing the difference in this ratio between oxidized and reduced states. For example, to compute the chemical strain perpendicular to the interface at 300°C for the reduced sample, the change in this ratio ([PCO y -spacing/YSZ y -spacing in reduced state] - [PCO y -spacing /YSZ y -spacing in oxidized state]) was computed and then divided by the ratio in the oxidized case, which gave the chemical strain perpendicular to the interface. This calculation assumed, consistent with expectations, that only PCO, and not YSZ, responded to oxidation or reduction conditions at high temperature. The lattice spacing in the YSZ for each condition was determined based on FFT analysis of the maximum square of available YSZ lattice adjacent to the PCO-YSZ interface. The position of the interface was identified by image contrast associated with defects at the interface as shown in Fig. 7. Between two and six squares of YSZ lattice were analyzed for each condition, with average side length 11-13 nm for Fig. 4 and 7 nm for Fig. 2(d). The choice to use YSZ as an internal reference length scale allowed control for image distortion due to tilt variation among different imaging conditions, while also providing a length scale robust to errors in the built-in scale bar of the TEM. Changes in defect chemistry based on observed strains were estimated by applying the chemical expansion coefficient of PCO ($\alpha_c = 0.087$) and Eq. 2.⁶

To improve image signal to noise ratio, images from the annealing study were stitched together using the pairwise stitching toolbox in Fiji.^{58,59} The width and periodic interfringe spacing for contrast fringes at the PCO-YSZ interface were analyzed using ImageJ, as de-

scribed in SI and Fig. S2.

EELS data were analyzed following the background subtraction procedure described by Bowman *et al.*⁴¹ and briefly summarized here. Background subtraction for the Ce peaks was conducted by fitting an exponential loss function to a 50 eV window that was positioned to end 5 eV below the Ce M5 peak. For the Pr peaks, background subtraction was done by a two-window procedure available in Digital Micrograph version 2, with a 5 eV window below the Pr M5 peak and a second window from 1120-1165 eV; that window was well beyond the high energy loss tail of Pr. The Ce M5 and M4 peak areas were measured based on integrating 20 and 25 eV fitting windows after background subtraction, respectively, spaced by 1 eV and starting at ~ 871 eV. The Pr M5 and M4 peaks were similarly characterized starting at 920 eV, and the full-width half-maximum (FWHM) of the Pr M5 peak was determined after applying a double-gaussian fit to the peak (after background subtraction) between 900 and 938 eV. This peak fitting was conducted using the curve-fitting toolbox in Matlab. The Cornell Spectrum Imager plugin for ImageJ was also used to handle, view and compare EELS spectrum image files and maps.^{60,61}

Time series data were fitted by linear regression. For the x -component lattice spacing, sufficient data density and range were available to apply a bootstrapping procedure to determine errors in fitting coefficients.⁶² Using a custom Matlab code, the slope and intercept of the linear fit of x -component lattice spacing *vs.* time was recomputed from 1000 resampled data sets to identify 95% confidence intervals for these parameters.

Acknowledgement

The authors gratefully acknowledge support from the U.S. Department of Energy, Basic Energy Sciences, Division of Materials Science and Engineering under award number DE-SC0002633 (Chemomechanics of Far-From-Equilibrium Interfaces, Program Manager J. Vetrano). J. G. Swallow thanks the Hugh Hampton Young Memorial Fund for fellowship

support. J. H. Warner thanks the support of the Royal Society and the EPSRC grant code EP/KO40375/1 for the South of England Analytical Electron Microscope. The authors thank H. Sawada for his assistance with TEM and EELS data collection, and B. Sheldon and S. Kumar for useful discussion.

Supporting Information Available

The following files are available free of charge.

- OxideTEM_SI.pdf: File containing additional discussion and characterization of interfacial structure, threading defects, *in situ* breathing, analysis methods, and a flow chart of high temperature experiments.

This material is available free of charge via the Internet at <http://pubs.acs.org/>.

References

1. Tuller, H. L.; Bishop, S. R. Point Defects in Oxides: Tailoring Materials Through Defect Engineering. *Annu. Rev. Mater. Res.* **2011**, *41*, 369–398.
2. Swallow, J. G.; Kim, J. J.; Maloney, J. M.; Chen, D.; Smith, J. F.; Bishop, S. R.; Tuller, H. L.; Van Vliet, K. J. Dynamic Chemical Expansion of Thin-Film Non-stoichiometric Oxides at Extreme Temperatures. *Nat. Mater.* **2017**, *16*, 749–754.
3. Garbayo, I.; Pla, D.; Morata, A.; Fonseca, L.; Sabaté, N.; Tarancón, A. Full Ceramic Micro Solid Oxide Fuel Cells: Towards More Reliable MEMS Power Generators Operating at High Temperatures. *Energy Environ. Sci.* **2014**, *7*, 3617–3629.
4. Sunarso, J.; Baumann, S.; Serra, J. M.; Meulenberg, W. A.; Liu, S.; Lin, Y. S.; Diniz da Costa, J. C. Mixed Ionic-Electronic Conducting (MIEC) Ceramic-Based Membranes for Oxygen Separation. *J. Membr. Sci.* **2008**, *320*, 13–41.

5. Perry, N. H.; Kim, J. J.; Bishop, S. R.; Tuller, H. L. Strongly Coupled Thermal and Chemical Expansion in the Perovskite Oxide System $\text{Sr}(\text{Ti,Fe})\text{O}_{3-\alpha}$. *J. Mater. Chem. A* **2015**, *3*, 3602–3611.
6. Bishop, S. R.; Tuller, H. L.; Kuru, Y.; Yildiz, B. Chemical Expansion of Nonstoichiometric $\text{Pr}_{0.1}\text{Ce}_{0.9}\text{O}_{2-\delta}$: Correlation With Defect Equilibrium Model. *J. Eur. Ceram. Soc.* **2011**, *31*, 2351–2356.
7. Mogni, L. V.; Prado, F. D.; Cuello, G. J.; Caneiro, A. Study of the Crystal Chemistry of the $n=2$ Ruddlesden-Popper Phases $\text{Sr}_3\text{FeMO}_{6+\delta}$ ($\text{M} = \text{Fe}, \text{Co}, \text{and Ni}$) Using *In Situ* High Temperature Neutron Powder Diffraction. *Chem. Mater.* **2009**, *21*, 2614–2623.
8. Atkinson, A.; Ramos, T. M. G. M. Chemically-Induced Stresses in Ceramic Oxygen Ion-Conducting Membranes. *Solid State Ionics* **2000**, *129*, 259–269.
9. Ahn, K.; Chung, Y.-C.; Yoon, K. J.; Son, J.-W.; Kim, B.-K.; Lee, H.-W.; Lee, J.-H. Lattice-Strain Effect on Oxygen Vacancy Formation in Gadolinium-Doped Ceria. *J. Electroceram.* **2014**, *32*, 72–77.
10. Kushima, A.; Yip, S.; Yildiz, B. Competing Strain Effects in Reactivity of LaCoO_3 with Oxygen. *Phys. Rev. B* **2010**, *82*, 115435.
11. Han, J. W.; Yildiz, B. Enhanced One Dimensional Mobility of Oxygen on Strained $\text{LaCoO}_3(001)$ Surface. *J. Mater. Chem.* **2011**, *21*, 18983–18990.
12. Yildiz, B. “Stretching” the Energy Landscape of Oxides—Effects on Electrocatalysis and Diffusion. *MRS Bull.* **2014**, *39*, 147–156.
13. Waser, R.; Dittmann, R.; Staikov, G.; Szot, K. Redox-Based Resistive Switching Memories - Nanoionic Mechanisms, Prospects, and Challenges. *Adv. Mater.* **2009**, *21*, 2632–2663.

14. Bishop, S. R.; Stefanik, T. S.; Tuller, H. L. Defects and Transport in $\text{Pr}_x\text{Ce}_{1-x}\text{O}_{2-\delta}$: Composition Trends. *J. Mater. Res.* **2012**, *27*, 2009–2016.
15. Chen, D.; Bishop, S. R.; Tuller, H. L. Praseodymium-Cerium Oxide Thin Film Cathodes: Study of Oxygen Reduction Reaction Kinetics. *J. Electroceram.* **2012**, *28*, 62–69.
16. Swallow, J. G.; Kim, J. J.; Kabir, M.; Smith, J. F.; Tuller, H. L.; Bishop, S. R.; Van Vliet, K. J. *Operando* Reduction of Elastic Modulus in $(\text{Pr,Ce})\text{O}_{2-\delta}$ Thin Films. *Acta Mater.* **2016**, *105*, 16–24.
17. Marrocchelli, D.; Bishop, S. R.; Tuller, H. L.; Yildiz, B. Understanding Chemical Expansion in Non-stoichiometric Oxides: Ceria and Zirconia Case Studies. *Adv. Funct. Mater.* **2012**, *22*, 1958–1965.
18. Marrocchelli, D.; Bishop, S. R.; Tuller, H. L.; Watson, G. W.; Yildiz, B. Charge Localization Increases Chemical Expansion in Cerium-Based Oxides. *Phys. Chem. Chem. Phys.* **2012**, *14*, 12070–12074.
19. Kuru, Y.; Marrocchelli, D.; Bishop, S. R.; Chen, D.; Yildiz, B.; Tuller, H. L. Anomalous Chemical Expansion Behavior of $\text{Pr}_{0.2}\text{Ce}_{0.8}\text{O}_{2-\delta}$ Thin Films Grown by Pulsed Laser Deposition. *J. Electrochem. Soc.* **2012**, *159*, F799–F803.
20. Sheth, J.; Chen, D.; Kim, J. J.; Bowman, W. J.; Crozier, P. A.; Tuller, H. L.; Mixture, S. T.; Zdziszynski, S.; Sheldon, B. W.; Bishop, S. R. Coupling of Strain, Stress, and Oxygen Non-stoichiometry in Thin Film $\text{Pr}_{0.1}\text{Ce}_{0.9}\text{O}_{2-\delta}$. *Nanoscale* **2016**, *8*, 16499–16510.
21. Grande, T.; Tolchard, J. R.; Selbach, S. M. Anisotropic Thermal and Chemical Expansion in Sr-Substituted $\text{LaMnO}_{3+\delta}$: Implications for Chemical Strain Relaxation. *Chem. Mater.* **2012**, *24*, 338–345.

22. Chen, X.; Grande, T. Anisotropic Chemical Expansion of $\text{La}_{1-x}\text{Sr}_x\text{CoO}_{3-\delta}$. *Chem. Mater.* **2013**, *25*, 927–934.
23. Chen, Q. N.; Adler, S. B.; Li, J. Imaging Space Charge Regions in Sm-Doped Ceria Using Electrochemical Strain Microscopy. *Appl. Phys. Lett.* **2014**, *105*, 201602.
24. Song, K.; Schmid, H.; Srot, V.; Gilardi, E.; Gregori, G.; Du, K.; Maier, J.; van Aken, P. A. Cerium Reduction at the Interface Between Ceria and Yttria-Stabilised Zirconia and Implications for Interfacial Oxygen Non-stoichiometry. *APL Mater.* **2014**, *2*, 032104.
25. Turner, S.; Lazar, S.; Freitag, B.; Egoavil, R.; Verbeeck, J.; Put, S.; Strauven, Y.; Van-Tendeloo, G. High Resolution Mapping of Surface Reduction in Ceria Nanoparticles. *Nanoscale* **2011**, *3*, 3385–3390.
26. Hailstone, R. K.; DiFrancesco, A. G.; Leong, J. G.; Allston, T. D.; Reed, K. J. A Study of Lattice Expansion in CeO_2 Nanoparticles by Transmission Electron Microscopy. *J. Phys. Chem. C* **2009**, *113*, 15155–15159.
27. Kim, Y.-M.; He, J.; Biegalski, M. D.; Ambaye, H.; Lauter, V.; Christen, H. M.; Pantelides, S. T.; Pennycook, S. J.; Kalinin, S. V.; Borisevich, A. Y. Probing Oxygen Vacancy Concentration and Homogeneity in Solid-Oxide Fuel-Cell Cathode Materials on the Subunit-Cell Level. *Nat. Mater.* **2012**, *11*, 888–894.
28. Sinclair, R. *In Situ* High-Resolution Transmission Electron Microscopy of Material Reactions. *MRS Bull.* **2013**, *38*, 1065–1071.
29. Borisevich, A. Y.; Chi, M.; Unocic, R. Functional Electron Microscopy for Electrochemistry Research: From the Atomic to the Micro Scale. *Electrochem. Soc. Interface* **2014**, 61–66.
30. Egerton, R. F. Electron Energy-Loss Spectroscopy in the TEM. *Rep. Prog. Phys.* **2009**, *72*, 016502.

31. Bowman, W. J.; March, K.; Hernandez, C. A.; Crozier, P. A. Measuring Bandgap States in Individual Non-stoichiometric Oxide Nanoparticles Using Monochromated STEM EELS: The Praseodymium-Ceria Case. *Ultramicroscopy* **2016**, *167*, 5–10.
32. Jang, J. H.; Kim, Y.-M.; He, Q.; Mishra, R.; Qiao, L.; Biegalski, M. D.; Lupini, A. R.; Pantelides, S. T.; Pennycook, S. J.; Kalinin, S. V.; Borisevich, A. Y. *In Situ* Observation of Oxygen Vacancy Dynamics and Ordering in the Epitaxial LaCoO₃ System. *ACS Nano* **2017**, *11*, 6942–6949.
33. Hÿtch, M. J.; Snoeck, E.; Kilaas, R. Quantitative Measurement of Displacement and Strain Fields From HREM Micrographs. *Ultramicroscopy* **1998**, *74*, 131–146.
34. Gong, C.; He, K.; Robertson, A. W.; Yoon, E.; Lee, G.-D.; Warner, J. H. Spatially Dependent Lattice Deformations for Dislocations at the Edges of Graphene. *ACS Nano* **2015**, *9*, 656–662.
35. Chen, D.; Bishop, S. R.; Tuller, H. L. Non-stoichiometry in Oxide Thin Films: A Chemical Capacitance Study of the Praseodymium-Cerium Oxide System. *Adv. Funct. Mater.* **2013**, *23*, 2168–2174.
36. Sinclair, R.; Lee, S. C.; Shi, Y.; Chueh, W. C. Structure and Chemistry of Epitaxial Ceria Thin Films on Ytria-Stabilized Zirconia Substrates, Studied by High Resolution Electron Microscopy. *Ultramicroscopy* **2017**, *176*, 200–211.
37. Chen, C. H.; Kiguchi, T.; Saiki, A.; Wakiya, N.; Shinozaki, K.; Mizutani, N. Characterization of Defect Type and Dislocation Density in Double Oxide Heteroepitaxial CeO₂/YSZ/Si(001) Films. *Appl. Phys. A: Mater. Sci. Process* **2003**, *76*, 969–973.
38. Gao, P.; Wang, Z.; Fu, W.; Liao, Z.; Liu, K.; Wang, W.; Bai, X.; Wang, E. *In Situ* TEM Studies of Oxygen Vacancy Migration for Electrically Induced Resistance Change Effect in Cerium Oxides. *Micron* **2010**, *41*, 301–305.

39. Cooper, D.; Baeumer, C.; Bernier, N.; Marchewka, A.; La Torre, C.; Dunin-Borkowski, R. E.; Menzel, S.; Waser, R.; Dittman, R. Anomalous Resistance Hysteresis in Oxide ReRAM: Oxygen Evolution and Reincorporation Revealed by *In Situ* TEM. *Adv. Mater.* **2017**, *6*, 1700212.
40. Crozier, P. A.; Wang, R.; Sharma, R. *In Situ* Environmental TEM Studies of Dynamic Changes in Cerium-Based Oxides Nanoparticles During Redox Processes. *Ultramicroscopy* **2008**, *108*, 1432–1440.
41. Bowman, W. J.; Zhu, J.; Sharma, R.; Crozier, P. A. Electrical Conductivity and Grain Boundary Composition of Gd-doped and Gd/Pr Co-doped Ceria. *Solid State Ionics* **2015**, *272*, 9–17.
42. Sun, L.; Marrocchelli, D.; Yildiz, B. Edge Dislocation Slows Down Oxide Ion Diffusion in Doped CeO₂ by Segregation of Charged Defects. *Nat. Commun.* **2015**, *6*, 1–10.
43. Chen, D.; Tuller, H. L. Voltage-Controlled Nonstoichiometry in Oxide Thin Films: Pr_{0.1}Ce_{0.9}O_{2-δ} Case Study. *Adv. Funct. Mater.* **2014**, *24*, 7638–7644.
44. López-Cartes, C.; Bernal, S.; Calvino, J. J.; Cauqui, M. A.; Blanco, G.; Pérez-Omil, J. A.; Pintado, J. M.; Helveg, S.; Hansen, P. L. *In Situ* Transmission Electron Microscopy Investigation of Ce(IV) and Pr(IV) Reducibility in a Rh (1%)/Ce_{0.8}Pr_{0.2}O_{2-x} Catalyst. *Chem. Commun.* **2003**, 644–645.
45. Sameshima, S.; Kawaminami, M.; Hirata, Y. Thermal Expansion of Rare-Earth-Doped Ceria Ceramics. *J. Ceram. Soc. Jpn.* **2002**, *110*, 597–600.
46. Hayashi, H.; Saitou, T.; Maruyama, N.; Inaba, H.; Kawamura, K.; Mori, M. Thermal expansion Coefficient of Yttria Stabilized Zirconia for Various Yttria Contents. *Solid State Ionics* **2005**, *176*, 613–619.

47. Bishop, S. R.; Stefanik, T. S.; Tuller, H. L. Electrical Conductivity and Defect Equilibria of $\text{Pr}_{0.1}\text{Ce}_{0.9}\text{O}_{2-\delta}$. *Phys. Chem. Chem. Phys.* **2011**, *13*, 10165–10173.
48. Maicaneanu, S. A.; Sayle, D. C.; Watson, G. W. Evolution and Atomistic Structure of Dislocations Defects and Clusters Within CeO_2 Supported on ZrO_2 . *Chem. Commun.* **2001**, 289–290.
49. Jia, B. W.; Tan, K. H.; Loke, W. K.; Wicaksono, S.; Yoon, S. F. Formation of Periodic Interfacial Misfit Dislocation Array at the InSb/GaAs Interface /emphvia Surface Anion Exchange. *J. Appl. Phys.* **2016**, *120*, 035301.
50. Huang, S. H.; Balakrishnan, G.; Khoshakhlagh, A.; Jallipalli, A.; Dawson, L. R.; Hufaker, D. L. Strain Relief by Periodic Misfit Arrays for Low Defect Density GaSb on GaAs. *Appl. Phys. Lett.* **2006**, *88*, 131911.
51. Kim, S. I.; Lee, K. H.; Mun, H. A.; Kim, H. S.; Hwang, S. W.; Roh, J. W.; Yang, D. J.; Shin, W. H.; Li, X. S.; Lee, Y. H.; Snyder, G. J.; Kim, S. W. Dense Dislocation Arrays Embedded in Grain Boundaries for High-Performance Bulk Thermoelectrics. *Science* **2015**, *348*, 109–114.
52. Marrocchelli, D.; Sun, L.; Yildiz, B. Dislocations in SrTiO_3 : Easy to Reduce but Not so Fast for Oxygen Transport. *J. Am. Chem. Soc.* **2015**, *137*, 4735–4748.
53. Ding, Y.; Chen, Y.; Pradel, K. C.; Liu, M.; Wang, Z. L. *In-Situ* Transmission Electron Microscopy Study of Oxygen Vacancy Ordering and Dislocation Annihilation in Undoped and Sm-Doped CeO_2 Ceramics During Redox Processes. *J. Appl. Phys.* **2016**, *120*, 214302.
54. Kakihana, M.; Yoshimura, M. Synthesis and Characteristics of Complex Multicomponent Oxides Prepared by Polymer Complex Method. *Bull. Chem. Soc. Jpn.* **1999**, *72*, 1427–1443.

55. Giannuzzi, L. A., Stevie, F. A., Eds. *Introduction to Focused Ion Beams: Instrumentation, Theory, Techniques and Practice*; Springer, 2005; Chapter 10.
56. Graff, A.; Simon, M.; Altmann, F. Using Enhanced SE Signal in the SEM for TEM Sample Thickness Determination. *Microsc. and Microanal.* **2007**, *13*, 98–99.
57. Mitchell, D. R. G. DiffTools: Electron Diffraction Software Tools for DigitalMicrographTM. *Microsc. Res. and Tech.* **2008**, *71*, 588–593.
58. Preibisch, S.; Saalfeld, S.; Tomancak, P. Globally Optimal Stitching of Tiled 3D Microscopic Image Aquisitions. *Bioinformatics* **2009**, *25*, 1463–1465.
59. Schindelin, J.; Arganda-Carreras, I.; Frise, E.; Kyanig, V.; Longair, M.; Pietzsch, T.; Preibisch, S.; Rueden, C.; Saalfeld, S.; Schmid, B.; Tinavez, J. Y.; White, D. J.; Hartenstein, V.; Eliceiri, K.; Tomancak, P.; Cardona, A. Fiji: An Open-Source Platform for Biological-Image Analysis. *Nat. Methods* **2012**, *9*, 676–682.
60. Schneider, C. A.; Rasband, W. S.; Eliceiri, K. W. NIH Image to ImageJ: 25 Years of Image Analysis. *Nat. Methods* **2012**, *9*, 671–675.
61. Hovden, R.; Cueva, P.; Mundy, J. A.; Muller, D. A. The Open-Source Cornell Spectrum Imager. *Microsc. Today* **2013**, *21*, 40–44.
62. Efron, B. In *Breakthroughs in Statistics*; Kotz, S., Johnson, N. L., Eds.; Springer, 1992; Chapter Bootstrap Methods: Another Look at the Jackknife.

Graphical TOC Entry

